Drivers of surface ocean acidity extremes in an Earth system model

Friedrich A. Burger[1,2] and Thomas L. Frölicher[1,2]

[1]Climate and Environmental Physics, Physics Institute, University of Bern, Bern, Switzerland.
[2]Oeschger Centre for Climate Change Research, University of Bern, Bern, Switzerland.

Key Points:

- The physical and biogeochemical drivers of surface ocean acidity extremes are analysed using high-frequency output of an Earth system model
- Higher temperatures due to enhanced ocean heat uptake drive the onset of high $[H^+]$ extremes in the subtropics
- In contrast, higher carbon concentrations due to increased vertical mixing and advection cause low Ω extremes in most regions

Corresponding author: Friedrich A. Burger, `friedrich.burger@unibe.ch`

Abstract

Oceanic uptake of anthropogenic carbon causes acidification, a process that describes the increase in hydrogen ion concentrations ([H^+]) and decrease in calcium carbonate mineral saturation states (Ω). Of particular concern are ocean acidity extreme (OAX) events, which pose a significant threat to many calcifying marine organisms. However, the mechanisms driving such extreme events are not well understood. Here, we use high-frequency output from a fully-coupled Earth system model of all processes that influence the surface ocean temperature and carbon budgets and ultimately [H^+] and Ω anomalies to quantify the driving mechanisms of the onset and decline of high [H^+] and low Ω extreme events. We show that enhanced temperature plays a crucial role in driving [H^+] extremes, with increased net ocean heat uptake being the dominant driver of the event onset in the subtropics. In the mid-to-high latitudes, decreased downward vertical diffusion and mixing of warm surface waters during summer, and increased vertical mixing with warm and carbon-rich subsurface waters during winter are the main drivers of high [H^+] extreme event onset. In the tropics, increases in vertical advection of carbon-rich subsurface waters are the primary driver of the onset of high [H^+] extremes. In contrast, low Ω extremes are driven in most regions by increases in surface carbon concentration due to increased vertical mixing with carbon-rich subsurface waters. Our study highlights the complex interplay between heat and carbon anomalies driving OAX events and provides a first foundation for more accurate prediction of their future evolution.

Plain Language Summary

Extreme events in ocean acidity and calcium carbonate saturation state may worsen the impacts from ocean acidification on marine ecosystems in the coming decades. Yet, the physical and biogeochemical drivers of such extreme events, such as air-sea CO_2 and heat exchange and vertical mixing, have not been analyzed. Based on high-frequency output of an Earth system model simulation, this study presents a first global assessment of the drivers of these extremes in the surface ocean. We find air-sea heat uptake and suppressed vertical mixing with colder subsurface waters to be major drivers of high [H^+] extremes in subtropical oceans and also in higher latitude regions during summer. There, increased vertical mixing is the major driver during winter, mixing up carbon-rich and warmer subsurface waters. In tropical regions, extremes in [H^+] are caused by upwelling of carbon-rich waters. In contrast, we find that extremes in calcium carbonate saturation state are mainly caused by increased vertical mixing or upwelling of carbon-rich deep waters.

1 Introduction

Since the beginning of the industrial era, the ocean has taken up 20 to 30 % of the anthropogenic carbon emissions (Friedlingstein et al., 2022). This uptake has caused changes in ocean chemistry, collectively known as ocean acidification (Caldeira & Wickett, 2003; Doney, Fabry, et al., 2009). Specifically, the pH of the surface ocean has decreased by approximately 0.12 since preindustrial times, corresponding to an increase in hydrogen ion concentration ([H^+]) by 30 % (Jiang et al., 2023). In addition, the concentration of carbonate ions ([CO_3^{2-}]) has decreased by about 16 %, which has resulted in a decrease in the saturation state of calcium carbonate (Ω) (Orr et al., 2005; Jiang et al., 2023). These changes are projected to continue and even accelerate in the future (Orr et al., 2005; Steinacher et al., 2009; Bopp et al., 2013; Kwiatkowski et al., 2020; Canadell et al., 2021). By the end of the 21st century, surface ocean [H^+] is projected to increase by another 4 - 150 % and [CO_3^{2-}] concentration is projected to decrease by another 2 - 48 %, depending on the future carbon emission scenario (Jiang et al., 2023). These ongoing changes in ocean chemistry are expected to have far-reaching implications for marine organisms and the services they provide to humanity (Kroeker et al., 2013; Doney et al., 2020; Bindoff et al., 2019).

Extreme variations in ocean acidity, known as OAX events, can amplify the impacts of long-term ocean acidification on marine organisms and ecosystems by pushing them beyond their limits of resilience (e.g., Spisla et al., 2021; Gruber et al., 2021; Bednaršek et al., 2022). These events can cause changes in hydrogen ion concentration ($[H^+]$) and other carbonate system variables of similar magnitude to those expected from long-term ocean acidification during the 21st century (Hofmann et al., 2011; Leinweber & Gruber, 2013; Desmet et al., 2022), particularly in coastal oceans (Torres et al., 2021). OAX events occur on much shorter timescales and can have detrimental impacts on marine organisms, as demonstrated, for example, by laboratory and field studies that show signs of shell dissolution in calcifying organisms after only a few days in undersaturated calcium carbonate waters (e.g., Bednaršek et al., 2012, 2014). These findings emphasize the need to consider both short-term and long-term impacts of extreme ocean acidity levels when assessing the health and sustainability of marine ecosystems.

OAX events are projected to become more frequent or even permanent due to long-term ocean acidification by the end of the 21st century (Burger et al., 2020). In addition, short-term departures from normal $[H^+]$ conditions are expected also to become larger in the future, since $[H^+]$ becomes more sensitive to variations in physical and biogeochemical ocean conditions as a consequence of the nonlinear nature of oceanic carbon chemistry (Orr et al., 2018; Fassbender et al., 2018; Kwiatkowski et al., 2023). For example, the frequency of $[H^+]$ extreme events relative to a shifting-mean baseline that includes long-term ocean acidification is projected to increase by a factor of 14 under a high emission scenario by the end of the century (Burger et al., 2020). Such increases in extreme departures may further increase the risk for marine ecosystems under ocean acidification, since ecosystems may be pushed earlier and more frequently beyond their limits of resilience. At the same time, variations in $[CO_3^-]$ and aragonite saturation state (Ω_A) are expected to become smaller, because $[CO_3^-]$ and Ω_A become less sensitive to variations in physical and biogeochemical ocean conditions (Orr et al., 2018; Burger et al., 2020).

Not only the projections of extreme deviations in $[H^+]$ and Ω_A from the long-term mean differ. It is also important to note that these extremes often occur independently from each other. For example, the 2013-2015 marine heatwave in the North Pacific, known as 'the Blob', was associated with extremely high $[H^+]$ conditions (Gruber et al., 2021), but not with extremely low Ω_A conditions (Mogen et al., 2022). This difference may be attributed to the fact that distinct drivers can cause $[H^+]$ and Ω_A extremes. While high $[H^+]$ levels and low Ω_A level may arise from increased dissolved inorganic carbon or decreased alkalinity, high $[H^+]$ levels may also be caused by elevated temperatures (Burger et al., 2022). Furthermore, the drivers determine whether acdification extremes co-occur with extremes in other stressors such as temperature. Understanding when these two types of acidification extremes do not coincide is crucial, particularly if expected impacts are primarily linked to one of the two variables.

Most available studies on OAX events have focused on examining their long-term changes under climate change (Burger et al., 2020; Hauri et al., 2013), as well as on identifying the drivers of the mean seasonal cycle (Hagens & Middelburg, 2016; Xue et al., 2021; Orr et al., 2022) and its changes (Kwiatkowski & Orr, 2018). However, the causes of large deviations in $[H^+]$ or Ω_A from their mean seasonal cycles during OAX events are currently unknown. These seasonal anomalies are likely driven by changes in temperature and dissolved inorganic carbon (Deser et al., 2010; Doney, Lima, et al., 2009), which are the most important driving variables. The contribution of different physical and biogeochemical processes, such as air-sea heat and CO_2 exchange and vertical mixing of heat and carbon, to changes in surface heat and carbon and ultimately to extremes in $[H^+]$ or Ω_A is currently unknown. A better understanding of these processes is crucial for making accurate predictions about the future evolution of OAX events at the regional scale (Burger et al., 2020).

In this study, the drivers of extreme events in $[H^+]$ and Ω_A in the global surface ocean are analyzed for the first time. The analysis is based on a pre-industrial control simulation of the GFDL ESM2M Earth system model. It makes use of a suite of model tendency terms for the carbon and temperature budgets that allows to decompose changes in temperature and carbon into contributions from the underlying physical and biogeochemical processes (Gnanadesikan et al., 2012; Palter et al., 2014; S. M. Griffies et al., 2015; Vogt et al., 2022). The remainder of this article is structured as follows. In section 2, the methods used to analyze the drivers of $[H^+]$ extremes are introduced. Section 3 presents the results, and a discussion of the results and conclusions are given in section 4.

2 Methods

2.1 Model and experimental design

This study is based on a preindustrial control simulation from the Earth system model GFDL ESM2M (Dunne et al., 2012, 2013). The GFDL ESM2M is a fully coupled carbon cycle-climate model that was developed at NOAA's Geophysical Fluid Dynamics Laboratory (GFDL). The model consists of an ocean (MOM4p1; S. Griffies, 2009), atmosphere (AM2; Anderson et al., 2004), land (LM3; Shevliakova et al., 2009) and sea ice (Winton, 2000) module. The Modular Ocean Model version 4p1 (MOM4p1) uses a grid with a horizontal nominal 1 ° resolution that increases near the equator to 0.3 ° and with a time-varying vertical resolution of about 10 m in the upper ocean. In this study, we analyze data for the uppermost vertical layer that extends from the surface to about 10 m depth. MOM4p1 is coupled to the ocean biogeochemistry model Tracers of Ocean Phytoplankton with Allometric Zooplankton version two (TOPAZv2; Dunne et al., 2013). TOPAZv2 simulates the cycling of 30 biogeochemical tracers, three phytoplankton groups, and zooplankton grazing. Carbonate chemistry follows the OCMIP2 recommendations (Najjar & Orr, 1998; Burger et al., 2020).

We used output of a 100 y preindustrial control simulation that was run under prescribed atmospheric CO_2 levels of 286 ppm (Vogt et al., 2022). Aerosol and solar forcing were also set to preindustrial 1860 values, and no anthropogenic land use and volcanic activity was assumed. We stored output for temperature (T), dissolved inorganic carbon (C_T), total alkalinity (A_T), salinity (S), silicate, and phosphate at two-hourly resolution, which is equivalent to the ocean model time step. By using *mocsy 2.0* (Orr & Epitalon, 2015), these data were used to calculate $[H^+]$ and the saturation states of aragonite Ω_A — a mineral form of calcium carbonate produced by marine organisms. $[H^+]$ and Ω_A were recalculated on the model time step because *mocsy 2.0* is also used to calculate partial derivatives of $[H^+]$ and Ω_A in the analysis (see section 2.4). This approach thus avoids slight inconsistencies between the carbonate chemistry representations of the ESM2M model and *mocsy 2.0*, increasing the accuracy of the analysis. The data were then aggregated to daily-mean resolution for the analysis. Additionally, output for the processes that modulate T and C_T - specifically T and C_T tendency terms - were also stored on two-hourly resolution. Storing tendency terms at each ocean model time step allowed to precisely calculate the changes in daily-mean T and C_T arising from the individual tendency terms.

2.2 Model evaluation

The findings of this study depend on the models' ability to accurately simulate the variations in $[H^+]$ and Ω_A anomalies. The GFDL ESM2M Earth system model, with its nominal 1° horizontal grid resolution in the ocean, is only suitable for assessing ocean acidity extremes on spatial scales of approximately 100 km and larger. The model is not well suited for driver analysis in coastal oceans and at local scales, since mesoscale and submesoscale variability (e.g., Desmet et al., 2022; Hayashida et al., 2020) are not well represented. To evaluate the simulated variability in the open ocean, we compare the model simulation with estimates of observation-based gridded data with a similar 1° horizontal resolution. The observation-based data, covering the period 1982-2021 (see also Burger et al., 2022), consists of the Hadley Centre EN4.2.2 objective analyses T and S fields (Good et al., 2013). Additionally, $[H^+]$ and Ω_A were calculated with CO2SYS using SOCAT-based fCO_2 (MPI-SOMFNN v2022; Landschützer et al., 2016; Landschützer et al., 2022) and total alkalinity calculated from S and T using the LIARv2 algorithm (Carter et al., 2018). Since the fCO_2 data is only available on monthly timescales, this model-data comparison is limited to monthly-mean resolution.

After removing the long-term linear trends from the observation-based data, we find a generally good agreement between simulated and observation-based variability of anomalies relative to the seasonal cycle in surface temperature and salinity (Figure 1). The pattern correlation coefficients of the standard deviation in anomalies are 0.53 for temperature and 0.50 for salinity. However, the model tends to overestimate temperature variability in the Southern Ocean (Figure 1a, e; supporting information Table S3) and salinity variability in the western tropical Pacific and Indian Ocean (Figure 1b, f). These biases suggest that the model may overestimate the contributions of temperature variations to extremes in the Southern Ocean and freshwater fluxes in the western tropical Pacific and Indian Ocean. We also find good agreement between simulated and observation-based spatial patterns of $[H^+]$ and Ω_A variability with pattern correlation coefficients of the standard deviation in $[H^+]$ and Ω_A anomalies of 0.48 and 0.62, respectively (Figure 1c,d,g,h). However, $[H^+]$ is generally more variable in the observation-based product compared to the model data (+33 % globally; supporting information Table S3), particularly in the high latitudes (e.g., +54 % in the Southern Ocean) and the eastern equatorial Pacific. The higher $[H^+]$ variability in the observation-based data is mainly attributable to the historical increase in $[H^+]$ sensitivity with respect to variations in its drivers from ocean acidification (Burger et al., 2020). Recalculating simulated $H^+]$ variability with the driving variables adjusted to the 1982-2021 mean conditions, which include ocean acidification and other historical trends, the excess in observation-based standard deviation is reduced to 4 % globally. However, an excess in observation-based standard deviation of $[H^+]$ anomalies remains in the high latitudes (+18 % over the Southern Ocean). Calculating observation-based C_T following the methodology for $[H^+]$ and Ω_A, we find that the remaining mismatch in these regions is associated with a negative bias in simulated variability in C_T anomalies (18 % smaller standard deviation in simulated C_T seasonal anomalies over the Southern Ocean). It is important to note the uncertainties in the observation-based data from the pCO2 mapping method (Fay et al., 2021), in particular in the high latitudes (Landschützer et al., 2016), highlighting a need to better constrain observation-based carbonate system variability.

In summary, we find a good agreement between simulated and observation-based variability of anomalies relative to the seasonal cycle in all analyzed variables, and a good match in the spatial variability patterns, despite a general low bias in simulated $[H^+]$ variability. These results suggest that the GFDL ESM2M model is well suited to analyze the drivers of extremes in $[H^+]$ and Ω_A in the open ocean.

2.3 Extreme event definition and identification of onset/decline periods

We examine events of both extremely high $[H^+]$ and extremely low Ω_A, which are collectively referred to as OAX events. We define OAX events based on seasonally-varying extreme event thresholds (Hobday et al., 2016; Vogt et al., 2022; Burger et al., 2022). At each location and for each day of the year, the $[H^+]$ extreme event threshold is determined as the 90th percentile of the 100 anomaly values with respect to the climatological seasonal cycle for that day of the year. As a result, the likelihood that the $[H^+]$

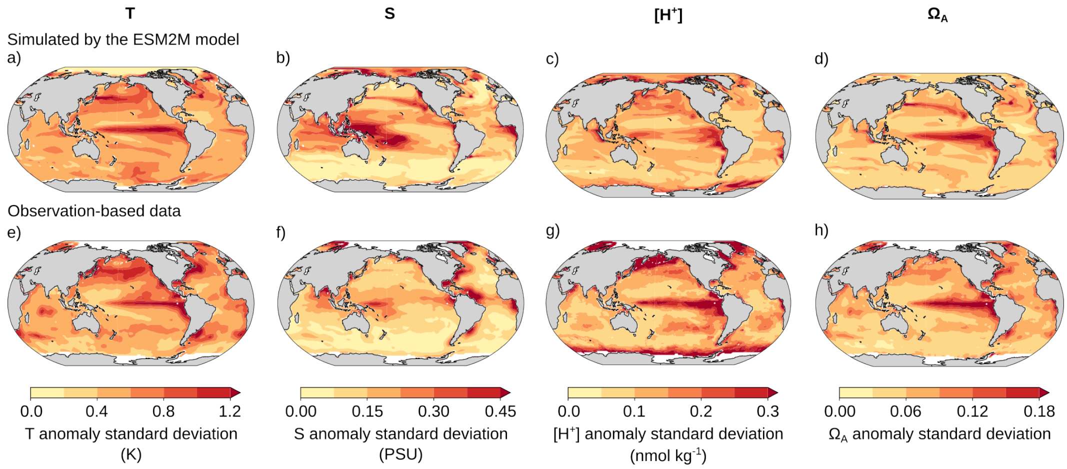

Figure 1. Standard deviation for anomalies relative to the seasonal cycle in (a,e) T, (b,f) S, (c,g) $[H^+]$, and (d,h) Ω_A, of the pre-industrial GFDL ESM2M model simulation (top) and observation-based data over the period 1982-2021 (bottom). The observation-based data was linearly detrended prior to the analysis.

anomaly exceeds the threshold is equal across locations and across the year. The choice of the 90th percentile ensures the inclusion of extreme ocean conditions while maintaining a sufficiently large sample for robust analyses. At a specific location, extreme events in $[H^+]$ are then defined as coherent periods over which the $[H^+]$ anomaly is above the local seasonally varying threshold (Figure 2). Similarly, extremely low Ω_A events are defined when Ω_A falls below the seasonally-varying thresholds that are given by the 10th percentiles of the anomaly distributions for each calendar day.

At each location and for each OAX event, we identify its onset and decline period (Figure 2). The onset phase is defined as the period between the start of the extreme event (e.g., where the $[H^+]$ anomaly exceeds the seasonally varying threshold) and the peak of the extreme event, where $[H^+]$ anomaly is maximal. Likewise, the decline phase is defined as the period between the peak of the extreme event and the time when $[H^+]$ anomaly falls below the threshold again. In this study, we average the change in $[H^+]$ anomaly and its drivers over these two periods. We assign the day of event peak to the decline period, as the change in $[H^+]$ anomaly on that day characterizes the reduction in $[H^+]$ anomaly between the peak day and the following day. Likewise, the last day of the decline period is excluded, as the change in $[H^+]$ anomaly on that day characterizes the transition from the last day of the event to the first day after the event.

2.4 Decomposition of OAX events into drivers

Changes in $[H^+]$ seasonal anomalies ($H^{+\prime}$) in each grid cell are decomposed into contributions from T, S, C_T and A_T (Figure 3; equation (1)). The change in $[H^+]$ anomaly between day i and day i+1, denoted by $\Delta H^{+\prime}(i)$, is approximated by employing a first order Taylor expansion of $[H^+]$ at day i, and by calculating the seasonal anomalies (denote by primes) of the obtained terms from T, C_T, A_T, and S:

$$\Delta H^{+\prime}(i) \simeq \underbrace{\left(\frac{\partial H^+}{\partial T}(i)\,\Delta T(i)\right)'}_{T\ term} + \underbrace{\left(\frac{\partial H^+}{\partial C_T}(i)\,\Delta C_T(i)\right)'}_{C_T\ term} + \underbrace{\left(\frac{\partial H^+}{\partial A_T}(i)\,\Delta A_T(i)\right)'}_{A_T\ term} + \underbrace{\left(\frac{\partial H^+}{\partial S}(i)\,\Delta S(i)\right)'}_{S\ term}. \quad (1)$$

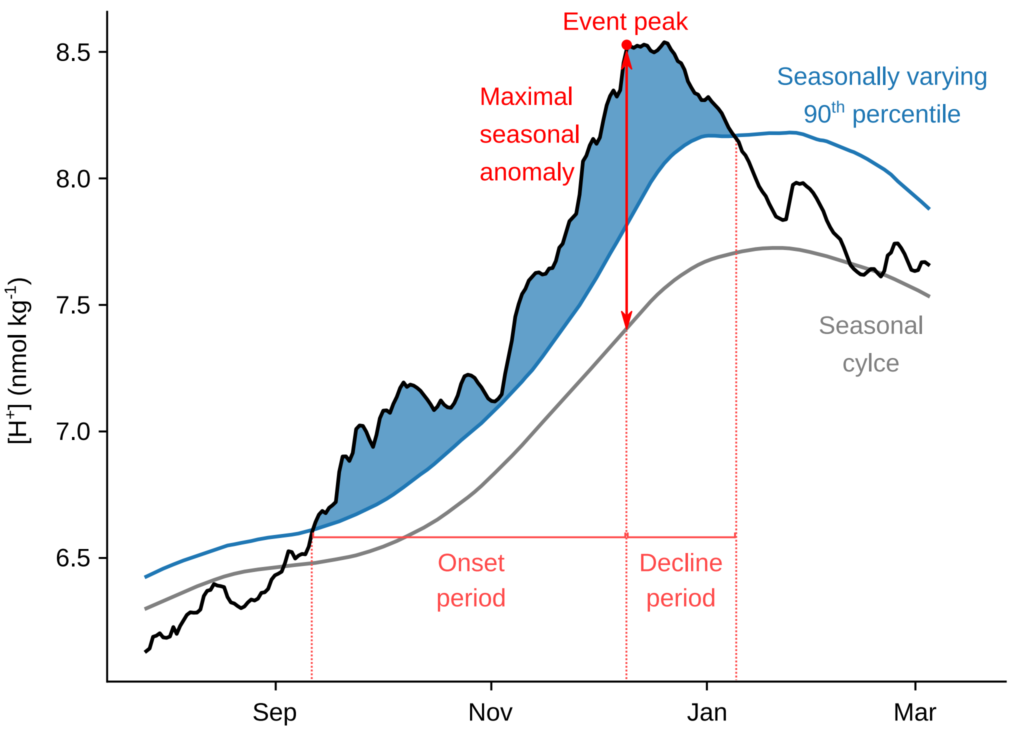

Figure 2. An exemplary $[H^+]$ extreme event in the northern subpolar Pacific depicting the event definition as well as the separation into event onset and decline periods.

$\Delta T(i)$, $\Delta C_T(i)$, $\Delta A_T(i)$, and $\Delta S(i)$ denote the changes in the respective variables between day i and day $i+1$. The partial derivatives with respect to T and C_T in equation (1) are calculated for each day from daily-mean T, C_T, A_T, S, silicate and phosphate using *mocsy* 2.0 (Orr & Epitalon, 2015). The analogous decomposition of anomaly changes is also performed for Ω_A.

The approximation of the changes in $[H^+]$ and Ω_A seasonal anomalies through the sum of the T, C_T, A_T, and S terms, as described in equation (1) for $[H^+]$, works well. For example, the root mean squared error (RMSE) over all simulated days of the approximation of $[H^+]$ anomaly change in equation (1) is $0.2\,\text{pmol kg}^{-1}\text{d}^{-1}$ ($\text{pmol} = 10^{-12}$ mol) on global average. RMSE is smaller than 5 % of the standard deviation of $[H^+]$ anomaly change over 99.9 % of the ocean, indicating that the approximation accurately captures variations in $[H^+]$ anomaly change.

2.5 Decomposition of T and C_T changes during OAX events into tendency terms

Within the ESM2M model, changes in T and C_T between two model time steps are calculated from a number of tendencies that describe the changes in T and C_T due to the individual physical and biogeochemical processes represented by the model (supporting information text S1; Palter et al., 2014; S. M. Griffies et al., 2015). We make use of these tendency terms to further decompose the changes in T and C_T into individual physical and biogeochemical drivers. To do so, changes in daily-mean T or C_T due to individual processes are reconstructed by adding up the respective tendency term on two-hourly (model time step) resolution between the two days that are considered (supporting information text S2).

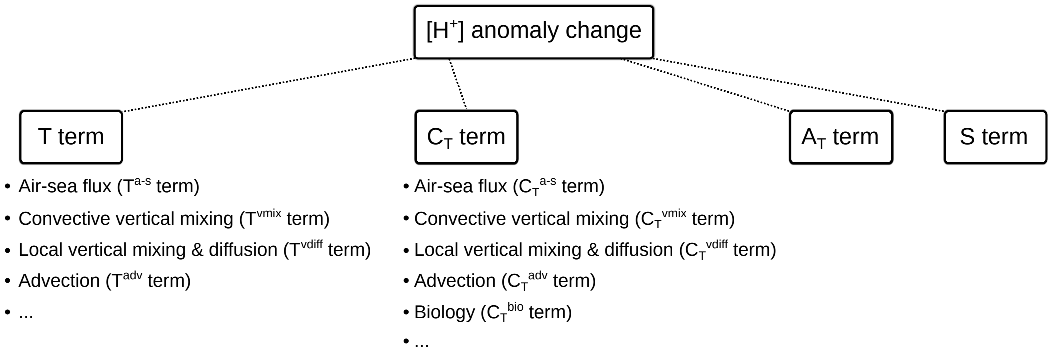

Figure 3. A scheme depicting the decomposition of $[\mathrm{H}^+]$ anomaly change ($\Delta \mathrm{H}^{+\prime}$) into the T, $\mathrm{C_T}$, $\mathrm{A_T}$, and S terms (equation (1)). The T and $\mathrm{C_T}$ terms are further decomposed into tendency contributions (equations (4) and (5)).

For temperature, these individual processes include air-sea exchange of heat ($\Delta \mathrm{T}^{\text{a-s}}$), resolved and parameterized subgrid-scale horizontal and vertical advection of heat ($\Delta \mathrm{T}^{\text{adv}}$), vertical diffusion and local mixing of heat (here referred to as *vertical diffusion* only; $\Delta \mathrm{T}^{\text{vdiff}}$), convective vertical mixing of heat in the ocean boundary layer as represented by the nonlocal KPP (K-profile) parametrization ($\Delta \mathrm{T}^{\text{vmix}}$), and a residual contribution ($\Delta \mathrm{T}^{\text{res}}$) from other processes, such as neutral diffusion and river runoff (supporting information text S1), as well as grid cell height variations (supporting information text S2):

$$\Delta \mathrm{T} \simeq \Delta \mathrm{T}^{\text{a-s}} + \Delta \mathrm{T}^{\text{vmix}} + \Delta \mathrm{T}^{\text{vdiff}} + \Delta \mathrm{T}^{\text{adv}} + \Delta \mathrm{T}^{\text{res}}. \tag{2}$$

Likewise, for $\mathrm{C_T}$ the contributions include air-sea exchange of $\mathrm{CO_2}$ ($\Delta \mathrm{C}_\mathrm{T}^{\text{a-s}}$), resolved and parameterized subgrid-scale horizontal and vertical advection of carbon ($\Delta \mathrm{C}_\mathrm{T}^{\text{adv}}$), vertical diffusion and local mixing of carbon ($\Delta \mathrm{C}_\mathrm{T}^{\text{vdiff}}$), nonlocal KPP convective mixing of carbon ($\Delta \mathrm{C}_\mathrm{T}^{\text{vmix}}$), biological carbon uptake and release ($\Delta \mathrm{C}_\mathrm{T}^{\text{bio}}$), and other processes including grid cell height variations ($\Delta \mathrm{C}_\mathrm{T}^{\text{res}}$):

$$\Delta \mathrm{C_T} \simeq \Delta \mathrm{C}_\mathrm{T}^{\text{a-s}} + \Delta \mathrm{C}_\mathrm{T}^{\text{vmix}} + \Delta \mathrm{C}_\mathrm{T}^{\text{vdiff}} + \Delta \mathrm{C}_\mathrm{T}^{\text{adv}} + \Delta \mathrm{C}_\mathrm{T}^{\text{bio}} + \Delta \mathrm{C}_\mathrm{T}^{\text{res}}. \tag{3}$$

More details on the individual tendencies and their underlying parametrizations can be found in supporting information text S1. The tendencies from grid cell height variations (part of the $\Delta \mathrm{T}^{\text{res}}$ and $\Delta \mathrm{C}_\mathrm{T}^{\text{res}}$ terms) do not represent physical or biogeochemical processes. However, they are needed to precisely reproduce $\Delta \mathrm{T}$ and $\Delta \mathrm{C_T}$ with equations (2) and (3). Based on equations (2) and (3), the T and $\mathrm{C_T}$ terms in equation (1) are decomposed into the individual tendency contributions:

$$\begin{aligned}\left(\frac{\partial \mathrm{H}^+}{\partial \mathrm{T}}(i)\,\Delta \mathrm{T}(i)\right)' = {} & \underbrace{\left(\frac{\partial \mathrm{H}^+}{\partial \mathrm{T}}(i)\,\Delta \mathrm{T}^{\text{a-s}}(i)\right)'}_{T^{a\text{-}s}\ term} + \underbrace{\left(\frac{\partial \mathrm{H}^+}{\partial \mathrm{T}}(i)\,\Delta \mathrm{T}^{\text{vmix}}(i)\right)'}_{T^{vmix}\ term} + \underbrace{\left(\frac{\partial \mathrm{H}^+}{\partial \mathrm{T}}(i)\,\Delta \mathrm{T}^{\text{vdiff}}(i)\right)'}_{T^{vdiff}\ term} \\ & + \underbrace{\left(\frac{\partial \mathrm{H}^+}{\partial \mathrm{T}}(i)\,\Delta \mathrm{T}^{\text{adv}}(i)\right)'}_{T^{adv}\ term} + \underbrace{\left(\frac{\partial \mathrm{H}^+}{\partial \mathrm{T}}(i)\,\Delta \mathrm{T}^{\text{res}}(i)\right)'}_{T^{res}\ term}\end{aligned} \tag{4}$$

$$\left(\frac{\partial \mathrm{H}^+}{\partial \mathrm{C_T}}(i)\,\Delta \mathrm{C_T}(i)\right)' = \underbrace{\left(\frac{\partial \mathrm{H}^+}{\partial \mathrm{C_T}}(i)\,\Delta \mathrm{C_T}^{\text{a-s}}(i)\right)'}_{C_T^{a\text{-}s}\ term} + \underbrace{\left(\frac{\partial \mathrm{H}^+}{\partial \mathrm{C_T}}(i)\,\Delta \mathrm{C_T}^{\text{vmix}}(i)\right)'}_{C_T^{vmix}\ term} + \underbrace{\left(\frac{\partial \mathrm{H}^+}{\partial \mathrm{C_T}}(i)\,\Delta \mathrm{C_T}^{\text{vdiff}}(i)\right)'}_{C_T^{vdiff}\ term}$$
$$+ \underbrace{\left(\frac{\partial \mathrm{H}^+}{\partial \mathrm{C_T}}(i)\,\Delta \mathrm{C_T}^{\text{adv}}(i)\right)'}_{C_T^{adv}\ term} + \underbrace{\left(\frac{\partial \mathrm{H}^+}{\partial \mathrm{C_T}}(i)\,\Delta \mathrm{C_T}^{\text{bio}}(i)\right)'}_{C_T^{bio}\ term} + \underbrace{\left(\frac{\partial \mathrm{H}^+}{\partial \mathrm{C_T}}(i)\,\Delta \mathrm{C_T}^{\text{res}}(i)\right)'}_{C_T^{res}\ term}. \tag{5}$$

The analogous decomposition is also performed for Ω_A.

3 Results

In Section 3.1, we quantify the contributions of the four drivers T, C_T, A_T, and S to the onset and decline of surface high [H^+] extremes. Subsequently, we evaluate the specific processes that modulate the impact of the two most important drivers, temperature (Section 3.2) and carbon concentrations (Section 3.3). We investigate the seasonal differences in these processes in Section 3.4. In Section 3.5, we briefly compare our findings on high [H^+] levels with those for low Ω_A extremes.

3.1 Contributions of temperature, carbon, alkalinity and salinity anomalies to the onset and decline of surface [H^+] extremes

On a global scale, the average increase in [H^+] anomalies during event onset is 9.1 pmol kg^{-1} d^{-1} (Table 1). The main factor contributing to the increase is the rise in temperature during the onset of the event. On a global scale, the temperature increase contributes 7.3 pmol kg^{-1} d^{-1}or 80% to the total increase. Increased temperature directly leads to an increase in [H^+] via changes in the carbonate chemistry equilibrium (Zeebe & Wolf-Gladrow, 2001). Increases in C_T also contribute to the increase in [H^+] globally, but the contribution of 2.4 pmol kg^{-1} d^{-1} is relatively small and accounts for 27% of the total [H^+] increase. Increases in alkalinity slightly counteract the [H^+] increases (-8 %) and contributions from changes in salinity are minor (1 %).

At the regional scale (Figure 4), we find that the increase in temperature is the dominant driver of [H^+] increases in 78 % of the global ocean surface area during the onset phase, whereas C_T dominates over 22 % of the ocean surface area. Regions that are particularly dominated by the C_T contribution are the eastern and central tropical Pacific and the Arctic Ocean. There, increases in [H^+] during the onset period result from increases in C_T (Figure 4e), while temperature decreases make the temperature contribution negative (Figure 4c). In the subtropics and the Southern Ocean, increases in temperature and associated increases in positive [H^+] anomalies are somewhat damped by decreases in C_T and associated decreases in [H^+] anomalies. In the Kuroshio and Gulf Stream regions and the Northern Indian Ocean, increases in [H^+] anomalies result from increases in both T (Figure 4c) and in C_T (Figure 4e). This pattern also holds true near Antarctica. However, it is important to note that the model may not adequately simulate physical and biogeochemical dynamics close to the Antarctic continent. The contribution from A_T is generally smaller and predominately opposite to the contribution of C_T (pattern correlation coefficient of -0.73). The A_T contribution is most important in the tropical regions where increases in A_T tend to decrease [H^+] and therefore inhibit event onset.

During the decline period of [H^+] extreme events, simulated reductions in temperature (Figure 4d) and C_T concentrations (Figure 4f) contribute similarly to the decline of [H^+] at the global scale, with a decrease of approximately -4.7 and -5.0 pmol kg^{-1} d^{-1}, respectively. This is in contrast to the onset period, where the temperature term dominates at the global scale. At the regional scale, the C_T term decreases almost everywhere

in $pmol\,kg^{-1}\,d^{-1}$		Global		Tropics		Subtropics		Southern Ocean	
		onset	**decline**	**onset**	**decline**	**onset**	**decline**	**onset**	**decline**
T	$T^{a\text{-}s}$ *term*	**12.6**	**-3.0**	**12.1**	**1.8**	**24.5**	**-6.3**	4.1	-0.9
	T^{vmix} *term*	**-9.5**	0.6	**-6.0**	-0.3	**-17.5**	**2.2**	**-6.0**	-1.5
	T^{vdiff} *term*	5.0	-1.8	-1.7	-2.1	3.2	-2.3	**11.7**	-1.6
	T^{adv} *term*	-0.6	-0.5	-1.3	-0.8	-2.0	-0.9	0.3	0.3
	T^{res} *term*	-0.1	0.0	-0.7	0.3	0.5	0.0	-0.1	-0.1
Sum of T terms		7.3	-4.7	2.6	-1.1	8.7	-7.3	10.0	-3.7
C_T	$C_T^{a\text{-}s}$ *term*	**-4.2**	**-5.3**	-3.3	**-3.8**	**-2.7**	**-3.7**	**-8.6**	**-9.6**
	C_T^{vmix} *term*	2.3	**2.3**	-0.1	**1.9**	**4.8**	**2.1**	2.4	**2.8**
	C_T^{vdiff} *term*	0.5	**1.7**	-0.8	0.8	-1.3	1.0	**4.3**	**4.1**
	C_T^{adv} *term*	**5.0**	-1.8	**16.6**	**-3.4**	-1.2	0.3	1.4	**-1.7**
	C_T^{bio} *term*	0.2	-1.0	**-3.4**	-2.9	0.2	0.0	0.9	-0.1
	C_T^{res} *term*	-1.3	-1.0	-2.0	-1.8	-0.3	-0.3	-0.5	-0.5
Sum of C_T terms		2.4	-5.0	6.9	-9.3	-0.4	-0.6	-0.1	-4.9
A_T term		-0.8	1.3	-2.0	3.4	0.1	-0.2	-0.2	0.6
S term		0.1	-0.2	0.3	-0.5	0.9	0.0	0.0	-0.1
Total		9.1	-8.5	7.8	-7.5	8.4	-8.1	9.8	-8.2
Simulated		9.1	-8.6	7.8	-7.5	8.4	-8.1	9.8	-8.2

Table 1. The simulated average daily changes in $[H^+]$ anomalies during the onset and decline periods of $[H^+]$ extreme events and the tendency contributions to these changes. Results are shown for the global ocean, the tropics, the subtropics, and the Southern Ocean. The regions are defined in Figure 4a. For each period and region, the two largest positive and negative contributions are highlighted in red and blue bold font, respectively. The T and C_T terms are decomposed into air-sea flux (*a-s*), convective vertical mixing (*vmix*), local vertical mixing and diffusion (*vdiff*), advection (*adv*), biology (*bio*), and residual (*res*) terms. 'Total' denotes the sum of all tendency contributions and 'Simulated' denotes the actual simulated $[H^+]$ change during the onset and decline phases.

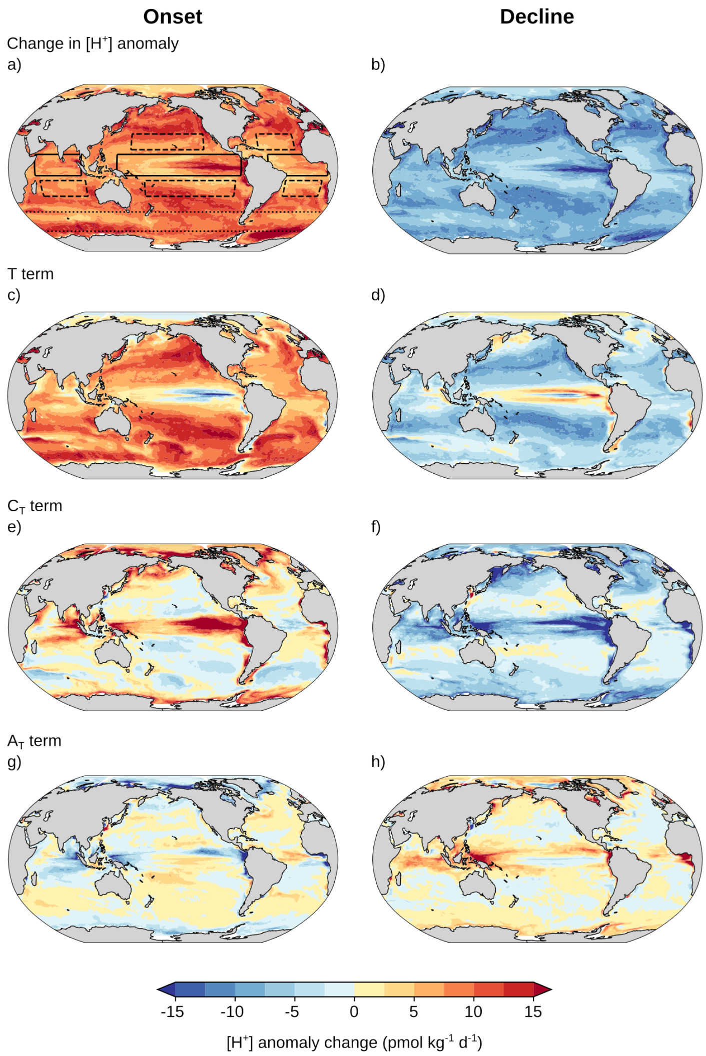

Figure 4. The simulated $[H^+]$ anomaly change during onset and decline of extreme high $[H^+]$ events and the contributions from the T, C_T, and A_T terms. (a, b) The simulated change in $[H^+]$ anomalies during the onset and decline phases of extreme $[H^+]$ events, the contribution of the (c, d) T term, (e, f) C_T term, and (g, h) A_T term (see equation (1)). The salinity term is small and not shown (see also Table 1). The solid, dashed, and dotted boxes in a) indicate the tropics (10 °S - 10 °N and 220 °W - 85 °W in the Pacific, 55 °W - 10 °E in the Atlantic, and 50 °E - 100 °E in the Indian Ocean), the subtropics (15 °N - 30 °N and 205 °W - 125 °W in the North Pacific, 30 °S - 15 °S and 190 °W - 90 °W in the South Pacific, 15 °N - 30 °N and 65 °W - 25 °W in the North Atlantic, 30 °S - 15 °S and 35 °W - 5 °E in the South Atlantic, and 30 °S - 15 °S and 55 °E - 105 °E in the Indian Ocean), and the Southern Ocean (65 °S - 45 °S), respectively. These regions are used in Table 1.

(in 94 % of the ocean surface area), with the largest decreases simulated in the tropical Pacific and the high latitudes (Figure 4f). Similarly, the temperature term also decreases in most regions (in 92 % of the surface ocean), with the most pronounced decreases in the subtropics (Figure 4d), where the temperature term is the main driver of [H$^+$] decline. An exception is again the equatorial Pacific, where temperature increases during the decline period of [H$^+$] extremes, thereby counteracting event decline.

3.2 Drivers of temperature variations during [H$^+$] extreme events

To understand the individual processes driving the changes in temperature anomalies during [H$^+$] extreme events and hence the temperature contribution to onset and decline of [H$^+$] extreme events (Figure 4c, d), the change in temperature anomaly during event onset and decline is decomposed (see equation (4); Table 1) into the contributions from air-sea heat exchange (Figure 5b, c), nonlocal KPP convective mixing (Figure 5e, f), vertical diffusion and local mixing (Figure 5h, i), and horizontal and vertical advection (Figure 5k, l). For ease of interpretation of the anomaly patterns, we also show the climatological means of the tendency contributions to the T term (Figure 5a,d,g,j). These are determined by calculating the temporal mean values of the tendency contributions to the T term instead of calculating their seasonal anomalies.

At the global scale, reduced ocean heat loss (i.e., net ocean heat uptake) contributes most to the increases in temperature anomalies during the onset period of [H$^+$] extreme events (Table 1). The net ocean heat uptake increases [H$^+$] anomalies by 12.6 pmol kg^{-1} d^{-1} (138 % of [H$^+$] anomaly increase) at the global scale. In addition, increases in temperature anomaly associated with reduced vertical diffusion and local mixing of warm waters to the subsurface cause an increase in [H$^+$] anomalies of 5.0 pmol kg^{-1} d^{-1} (54¸,% of [H$^+$] anomaly increase) during the onset period. Convective mixing increases sea surface temperature by transporting heat to the surface when surface waters lose buoyancy due to heat loss to the atmosphere. This mechanism is less active during the positive air-sea heat flux anomalies in the onset period. The associated negative anomalies in nonlocal KPP convective mixing during the onset period reduce surface temperature anomalies and therefore [H$^+$] anomalies during the onset, strongly dampening the temperature-induced increases in [H$^+$] anomalies (-9.5 pmol kg^{-1} d^{-1}, -104 % of [H$^+$] anomaly increase).

At the regional scale (Figure 5), the positive contribution from air-sea heat exchange is largest in the low-to-mid latitudes and in particular in the subtropical oceans (Table 1; Figure 5b), while the contribution is much smaller or negative in the high latitudes. In the subtropics, air-sea heat exchange often changes the sign from net loss to the atmosphere to net uptake during [H$^+$] extreme events (Figure 5a,b). Vertical diffusion and local mixing increases temperature anomaly and hence contributes positively to the T term in all ocean regions, except in the tropical Pacific and Indian Ocean, where vertical diffusion and local mixing of heat to the subsurface is increased during [H$^+$] extreme events (Figure 5h). The vertical diffusion and local mixing contribution is most positive in the North Atlantic, North Pacific, and Southern Ocean (Table 1, Figure 5h). In the subtropics and the mid-to-high latitudes during summer, the positive contribution from vertical diffusion and local mixing arises due to a reduction in mixing with colder subsurface waters that coincides with a reduction in wind strength (supporting information Figure S3a, c). In the high latitudes during winter, the positive contribution instead often arises due to an increase in upward mixing of heat. The increase in upward mixing of heat is associated with stronger winds (supporting information Figure S3c). Decreases in nonlocal KPP convective mixing decrease surface temperature and [H$^+$] almost in the entire global surface ocean, especially in the subtropics (Table 1, Figure 5e), where also increases in temperature anomaly due to air-sea heat exchange are largest (Figure 2b, Figure 5b). The contribution from advective heat transport is generally small (Figure 5k), except in the tropical Pacific, where it decreases temperature and [H$^+$] during the onset of [H$^+$] extreme events (Table 1, Figure 5e).

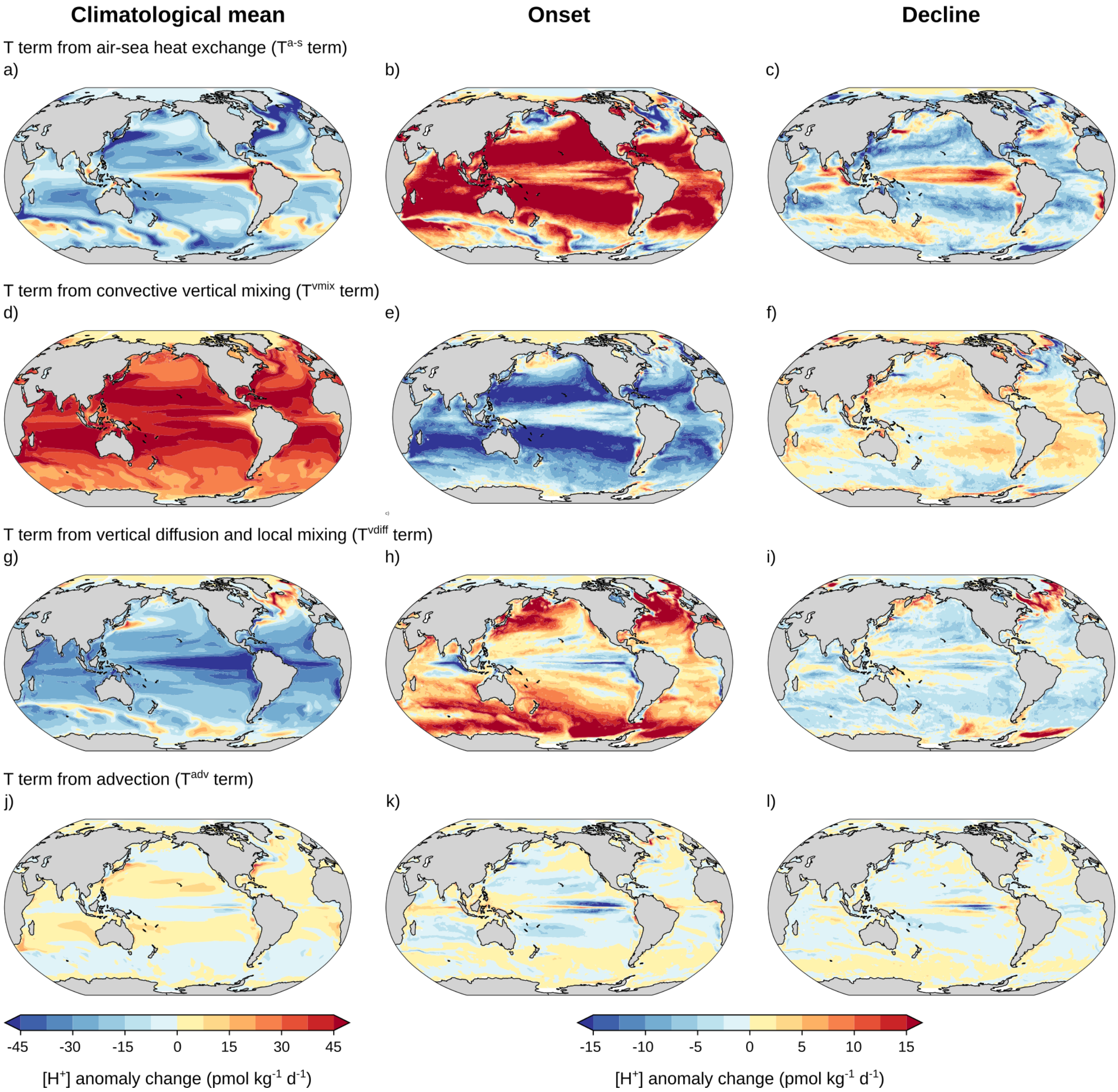

Figure 5. The decomposition of the T term into tendency contributions. The climatological means of the tendency contributions to the T term (first column) as well as their contributions to the onset (second column) and decline (third column) means of the T term (Figure 4 c, d).

During the decline phase of $[H^+]$ extreme events, the temperature decrease in the subtropics mainly results from increased heat losses to the atmosphere (Figure 5c). Vertical diffusion and local mixing also decreases temperature over most of the ocean (Figure 5i) and is the main driver of temperature decrease in the Southern Ocean (Table 1). The increases in temperature that counteract the $[H^+]$ event decline in the tropical Pacific (Figure 4d) result from enhanced ocean heat uptake during the decline phase (Figure 5c).

3.3 Drivers of carbon variations during $[H^+]$ extreme events

At the global scale (Table 1), vertical and horizontal advection is the most important driver of C_T increase during the onset of $[H^+]$ extreme events, increasing $[H^+]$ anomaly by $5.0\,\mathrm{pmol\,kg^{-1}\,d^{-1}}$ (55 % of $[H^+]$ anomaly increase). In addition, reduced nonlocal KPP convective vertical mixing of carbon increases $[H^+]$ by $2.3\,\mathrm{pmol\,kg^{-1}\,d^{-1}}$ (25 % of $[H^+]$ anomaly increase). These increases are balanced by decreases in C_T anomalies from negative anomalies in air-sea CO_2 flux during the onset of $[H^+]$ extreme events ($-4.2\,\mathrm{pmol\,kg^{-1}\,d^{-1}}$, -46 % of $[H^+]$ anomaly increase). Negative anomalies in air-sea CO_2 flux, i.e., increased carbon loss to the atmosphere or decreased CO_2 uptake from the atmosphere (Figure 6a), occur when partial pressure of CO_2 ($p\mathrm{CO_2}$) in the surface water is increased. Due to the high correlation between $[H^+]$ and $p\mathrm{CO_2}$ anomalies (Pearson correlation coefficient of 0.99 on global average in the model), negative anomalies in air-sea CO_2 flux during high $[H^+]$ events are expected. The contributions from vertical diffusion, local mixing and biology are small at the global scale. The residual term for C_T is larger than for T and mainly stems from neutral diffusion and a tendency that compensates a numerical artifact associated with the smoothing of the free ocean surface in the model.

At the regional scale (Figure 6), the contribution from vertical and horizontal advection to the onset of $[H^+]$ extreme events is largest in the tropics (Figure 6k, Table 1). Smaller positive contributions from advection are also simulated in high-latitude regions. However, the advection contribution is slightly negative in the subtropics. In the ESM2M model, C_T changes due to advection also include the diluting or concentrating effect on C_T from precipitation minus evaporation (Supporting information text S3). Negative precipitation minus evaporation anomalies (i.e., more evaporation than precipitation) increase C_T during event onset in the western tropical Pacific and Indian Ocean (Figure S4e), while the advective increases in C_T in the remaining tropics result from oceanic advection such as upwelling (supporting information Figure S4h), in particular in the eastern tropical Pacific where also advective decreases in temperature are simulated (Figure 5k). The slightly negative contribution from advection in the subtropics is caused by positive precipitation minus evaporation anomalies during the onset of $[H^+]$ extreme events.

The negative anomalies in air-sea CO_2 flux are largest in the high latitudes (Figure 6b). The anomalies in air-sea CO_2 exchange are offset by opposing tendencies from nonlocal KPP convective mixing of carbon in most regions (Figure 6e). The convective mixing increases C_T and $[H^+]$ everywhere except in the western tropical Pacific and the tropical Indian Ocean. Vertical diffusion and local mixing generally increase surface C_T in the climatological mean (Figure 6g). During the onset of $[H^+]$ extreme events, negative anomalies in vertical diffusion and local mixing counteract increases in $[H^+]$ anomaly in the subtropics, the mid latitudes, and most tropical regions (Figure 6h). In contrast, vertical diffusion and local mixing increases $[H^+]$ anomalies in the eastern tropical Pacific, and in high-latitude regions of the the North Pacific, North Atlantic, and Southern Ocean. Its contribution tends to be opposite to that of temperature vertical diffusion and local mixing due to opposite vertical gradients in temperature and C_T. This is not the case in the high-latitude regions where temperature and C_T vertical gradients are often both positive towards depth during the winter months. The reductions in vertical diffusion and local mixing of temperature and C_T (increasing temperature and de-

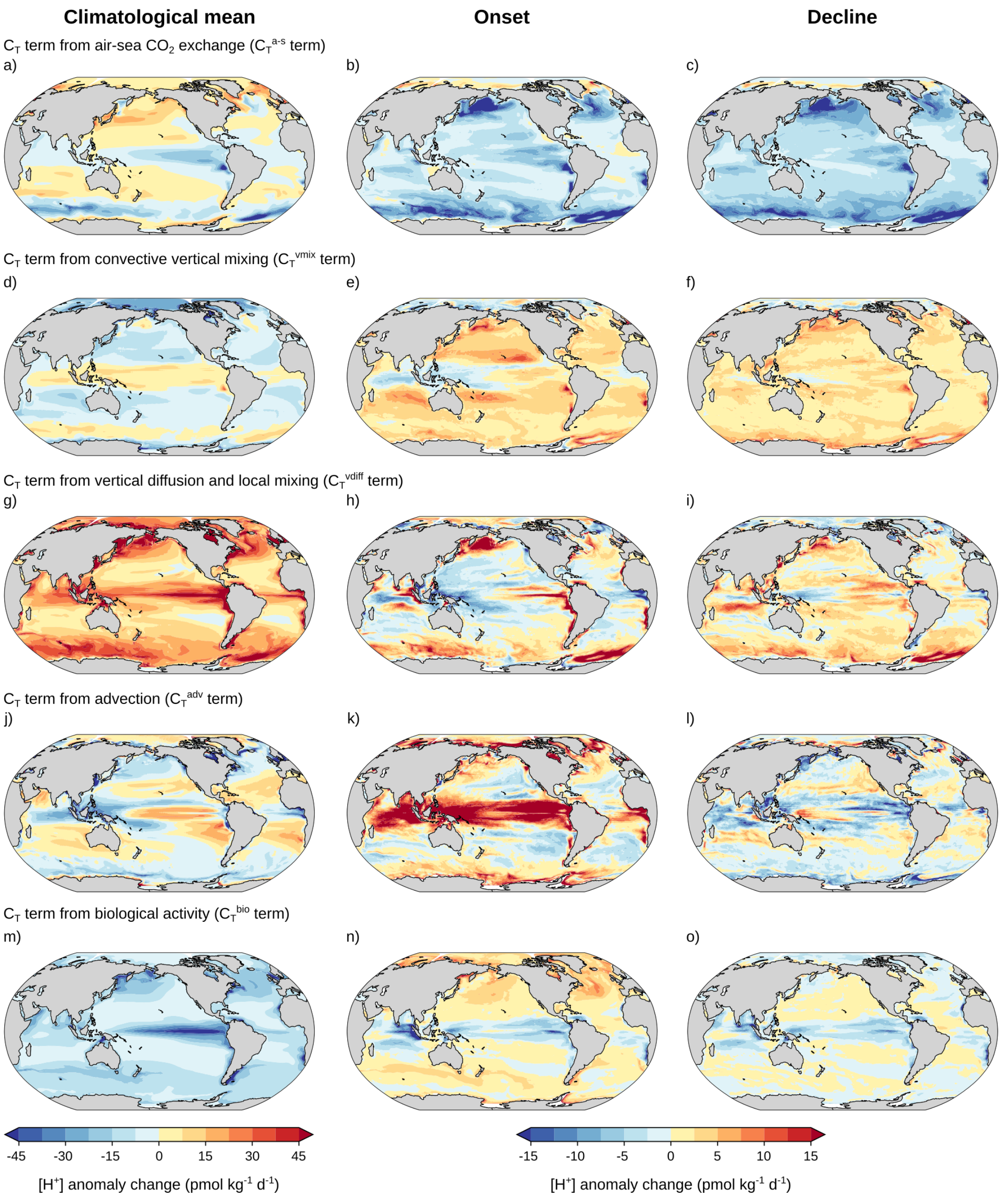

Figure 6. The decomposition of the C_T term into tendency contributions. The climatological means of the tendency contributions to the C_T term (first column) as well as their contributions to the onset (second column) and decline (third column) means of the C_T term (Figure 4 e, f).

creasing C_T) in the low-to-mid latitudes coincide with negative anomalies in wind stress during event onset (supporting information Figure S3a, c). In the high-latitude regions where positive anomalies in vertical diffusion and local mixing of temperature and C_T are simulated (Figures 5h and 6h), also wind stress and mixed layer depth (not shown) are increased during event onset, in particular during winter (supporting information Figure S3c). The increased wind stress may be the reason for enhanced vertical mixing during event onset in these regions.

Biological activity generally reduces C_T everywhere, because biological production outweighs decomposition at the surface (Figure 6m). During the onset of $[H^+]$ extreme events, increases in biological production decrease $[H^+]$ anomaly in the tropics (Table 1), while reductions in biological production increase $[H^+]$ anomaly in the mid-to-high latitudes (Figure 6n). In the tropical regions, increased nutrient concentrations are simulated during OAX events (not shown), which may cause increased phytoplankton growth there. In the mid-to-high latitudes, low biological production may be connected to nutrient limitation and / or low phytoplankton biomass due to enhanced zooplankton grazing under the elevated temperatures.

During the decline phase of $[H^+]$ extremes, C_T anomaly decreases almost in the entire ocean (Figure 4f). This decrease is mainly due to loss of carbon to the atmosphere (Figure 6c), which remains similarly strong as during the onset phase. In the tropical ocean, biological production continues to decrease C_T anomaly during event decline (Figure 6o), and also advection reduces C_T anomaly during event decline there (Figure 6c). The convective mixing term balances the carbon losses from air-sea gas exchange and counteracts $[H^+]$ event decline everywhere in the ocean (Figure 6f), and also vertical diffusion and local mixing increases $[H^+]$ anomaly during event decline in most regions (Figure 6i). These increases in vertical mixing, simultaneously also causing temperature decreases in the low-to-mid latitudes (Figure 5i), may be connected to the anomalous heat losses to the atmosphere (Figure 5c), causing loss of buoyancy.

3.4 Seasonal variations in drivers of $[H^+]$ extreme event onset

Next, we analyze if the drivers of $[H^+]$ extreme event onset differ between summer and winter season. At the global scale, the changes in $[H^+]$ anomaly per day during extreme event onset are by a factor of two larger during hemispheric summer (April to September on the northern and October to March on the southern hemisphere) than during hemispheric winter (October to March on the northern and April to September on the southern hemisphere; grey bars in Figure 7a). This difference arises from distinct drivers of $[H^+]$ extreme events during individual seasons. Globally, temperature changes are the dominant driver for event onset during the summer months, with $11.8\,\mathrm{pmol\,kg^{-1}\,d^{-1}}$ for temperature vs $1.0\,\mathrm{pmol\,kg^{-1}\,d^{-1}}$ for C_T. In contrast, C_T changes become more important in winter, with $3.9\,\mathrm{pmol\,kg^{-1}\,d^{-1}}$ for C_T vs $2.7\,\mathrm{pmol\,kg^{-1}\,d^{-1}}$ for temperature (Figure 7a).

In the tropics, temperature and C_T are both important drivers during hemispheric summer, but C_T is the dominant driver during hemispheric winter (Figure 7b). The smaller contribution from temperature in winter is due to lower net ocean heat uptake and increased heat loss from vertical diffusion and local mixing and advection. The larger contribution from C_T in winter, on the other hand, is due to larger surface C_T increases from advection as well as vertical diffusion and local mixing (supporting information Figure S4b).

In the subtropics, temperature is the dominant driver of $[H^+]$ event onset throughout the year, while the contributions from the other drivers are negligible both in summer and winter (Figure 7c). The overall larger $[H^+]$ increases during event onset in summer result from a larger reduction in heat loss from vertical diffusion and local mixing in summer (supporting information Figure S4c).

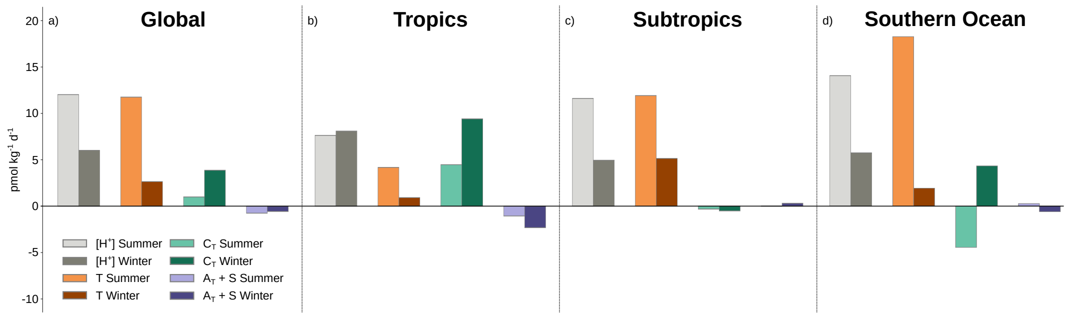

Figure 7. The contributions to $[H^+]$ extreme event onset (light and dark grey bars) from T (light and dark orange), C_T (light and dark green), and A_T and S (light and dark purple). Results are shown separately for hemispheric summer (April to September on the northern hemisphere and October to March on the southern hemisphere; light colors) and hemispheric winter (remaining months; dark colors). The definition of regions is shown in Figure 4a. Errors of the decomposition are not shown as they are very small (see Table 1).

In the Southern Ocean, the drivers during summer show similarities to subtropical regions, characterized by a large positive temperature contribution and a much smaller and negative C_T contribution (Figure 7d). The large positive temperature contribution is due to reduced vertical diffusion and local mixing with colder subsurface waters, associated with reduced winds (supporting information Figure S3a), and due to net ocean heat uptake. The negative C_T contribution is caused by reduced mixing with carbon-rich subsurface layers and due to air-sea CO_2 loss (supporting information Figure S4d). The regime is distinctly different during winter, where carbon increases are the main driver of event onset while temperature increases are only of secondary importance (Figure 7d). The increase in carbon is mainly caused by an increase in vertical diffusion and local mixing with carbon-rich subsurface layers that is associated to enhanced winds (supporting information Figure S3c). It is counteracted by amplified air-sea CO_2 loss to the atmosphere. The smaller positive contribution from temperature increases in winter is caused by enhanced vertical mixing and diffusion, transporting heat from the warmer subsurface to the surface (see also Section 3.2; supporting information Figure S4d).

3.5 Drivers of extremes in Ω_A

At the global scale, the onset of surface low Ω_A extremes is mainly caused by an increase in C_T, which accounts for 65 % of the total decrease in Ω_A (Figure 8a,b; supporting information Table S1). This is in contrast to high $[H^+]$ extremes, for which temperature accounts for 80 % of the total increase in $[H^+]$. The increase in C_T during low Ω_A extremes is primarily due to increased local vertical mixing and diffusion (Figure 8d), which is counterbalanced by enhanced biological activity, which decreases C_T (Figure 8f), as well as anomalous outgassing of CO_2 (Figure 8c). In addition, the decrease in total alkalinity (Figure 8g) and decrease in temperature from air-sea heat loss (Figure 8h,i) contribute to the decrease in Ω_A during event onset.

At the regional scale, the primary driver of the onset of low Ω_A extremes is the increase in C_T over most of the tropics and the Southern Ocean (Figure 8b; supporting information Table S1). The increase in C_T contributes 71% to the total decrease in Ω_A in the tropics and 99 % in the Southern Ocean. These increases in C_T are caused by enhanced vertical mixing and diffusion (Figure 8d), as well as advection of carbon-rich waters (Figure 8e). However, these increases in C_T in the tropics and the Southern Ocean are somewhat counterbalanced by decreases in carbon from anomalous CO_2 outgassing

(Figure 8c). Enhanced biological activity also decreases carbon in the tropics (Figure 8f). In the western tropical Pacific, the decrease in C_T is driven by the decrease in A_T (Figure 8g) resulting from enhanced precipitation (supporting information Figure S9b). Decreases in A_T are also contributing to the decreases in Ω_A in the subtropical regions, presumably due to enhanced vertical mixing with low-A_T subsurface waters. In addition, decreases in temperature from air-sea heat loss contribute to the decreases in Ω_A in the subtropics (Figure 8i).

The global decline of surface low Ω_A is mainly caused by decreases in C_T (predominantly from biological uptake of carbon), increases in A_T, and a smaller contribution from increasing temperatures that are caused by surface warming (supporting information Table S1).

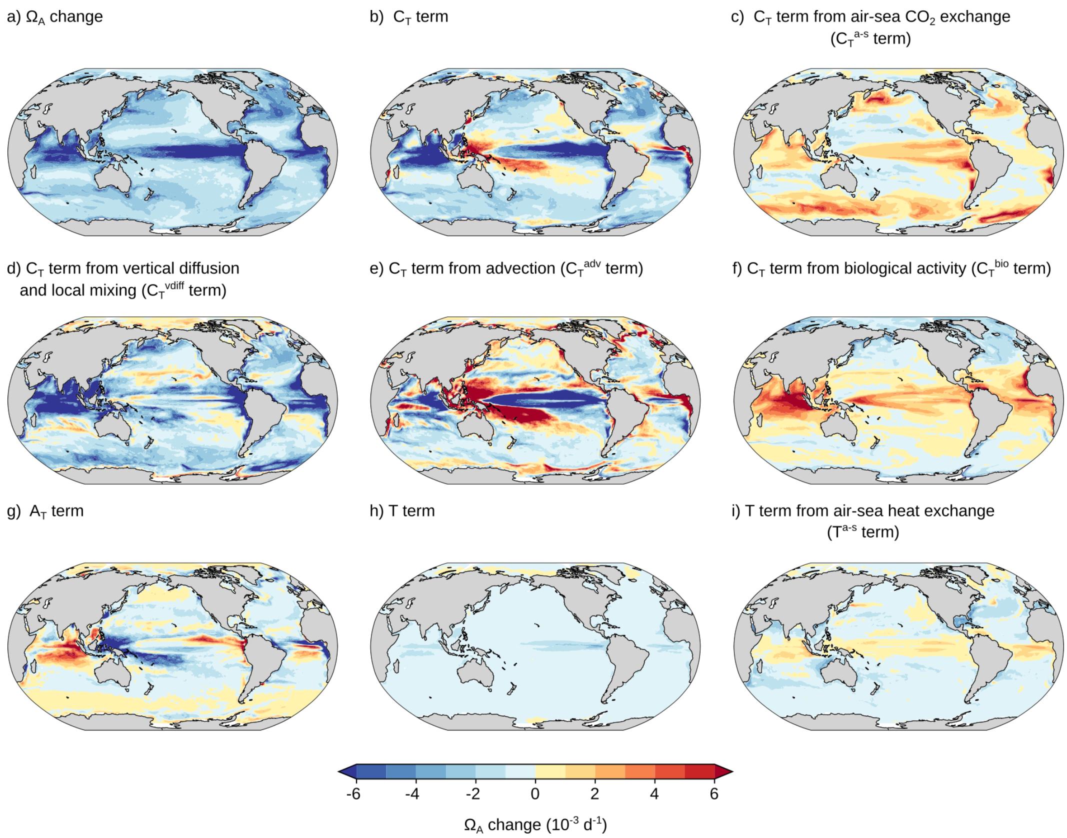

Figure 8. The Ω_A anomaly change during the onset phase of low Ω_A events, the contributions from the T, C_T, and A_T terms, and the most important tendency contributions to these. (a) The simulated change in Ω_A anomalies during the onset phase. (b-f) The contribution from the C_T term (b) and its air-sea CO_2 exchange (c), local vertical mixing and diffusion (d), advection (e), and biology (f) contributions. (g) The A_T term, and (h) the T term and its contribution from air-sea heat exchange (i). The salinity term and the other tendency contributions are smaller and not shown (see also supporting information Table S1). Blue colors indicate a decrease in Ω_A and thus an intensification of low Ω_A extremes.

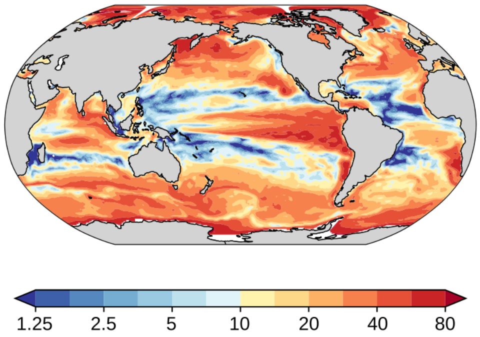

Figure 9. Overlap percentage of high $[H^+]$ and low Ω_A extremes. It is calculated as the number of days with co-occurring high $[H^+]$ and low Ω_A extremes divided by the number of days with high $[H^+]$ or low Ω_A extremes (10 % of days). Cold and warm colors indicate that the events coincide less and more frequent than by chance, respectively.

4 Discussion and conclusions

We provide a first assessment of the drivers of surface high $[H^+]$ and low Ω_A extreme events using high-frequency output of a comprehensive Earth system model. The results of this modeling study suggest that rising temperatures from enhanced net ocean heat uptake and reduced heat loss through vertical mixing are the primary drivers of high $[H^+]$ events in the subtropical regions and mid-to-high latitudes during summer. In tropical regions, simulated high $[H^+]$ events as well as low Ω_A events are often driven by increases in dissolved inorganic carbon due to advection. In mid-to-high latitudes during winter, we also find increased vertical mixing with carbon-rich and often warmer subsurface waters to be an important factor for the onset of high $[H^+]$ events.

Recent studies have investigated the biogeochemical imprint of the 2013-2015 marine heatwave in the North Pacific, known as the Blob. While extremely high $[H^+]$ was identified, the levels of Ω_A were not lower than usual, despite both being referred to as OAX events (Gruber et al., 2021; Mogen et al., 2022). Our study offers an explanation for this apparent contradiction: high $[H^+]$ events are often driven by temperature increases, in particular in the North Pacific region where the Blob occurred (Figure 3c), which suggests that the Blob was indeed an $[H^+]$ extreme. On the other hand, low Ω_A events usually coincide with periods of decreasing temperature (Figure 7e) and thus unlikely to coincide with MHWs.

The main driver of low Ω_A extremes in the model is an increase in C_T resulting from vertical mixing, diffusion, and advection, particularly in the tropics and the mid-to-high latitudes (Figure 7d,e). Similarly, advective increases in C_T were also identified as the main driver of $[H^+]$ in the tropics, and vertical diffusion and local mixing was identified as an important driver of $[H^+]$ extremes in the mid-to-high latitudes, in particular during winter (section 3.3). The resemblance in the driving mechanisms in these regions reflects in relatively frequent co-occurrence of simulated high $[H^+]$ and low Ω_A extremes: 26 % of high $[H^+]$ extreme days overlap with low Ω_A extreme days in the tropics and 31 % of event days overlap in the Southern Ocean (Figure 9), in particular during winter where 43 % of event days coincide. In contrast, the driving mechanisms diverge in the subtropics, reflected in a relatively low overlap of event days of only 11 % there (Figure 9).

Our study suggests that temperature increase is the main driver of $[H^+]$ extremes in the subtropics, which may share similar physical drivers to those of marine heatwaves. Using the same GFDL ESM2M model, Vogt et al. (2022) found that air-sea heat fluxes were the main factor responsible for temperature increases during the onset of marine heatwaves, particularly in the subtropical oceans, offset by temperature decreases resulting from reduced nonlocal-KPP convective mixing (Figure 1 in Vogt et al., 2022). Our findings are thus consistent with those of Vogt et al. (2022) for the subtropical oceans. During the onset period, anomalous air-sea heat flux was identified as the primary driver of $[H^+]$ increase, and likewise, during event decline, air-sea heat flux was the main driver of $[H^+]$ decrease (Figure 5b, c; Table 1). Moreover, reduced convective mixing from the nonlocal KPP parameterization was identified as the primary inhibiting factor during the onset period, and to a lesser extent, also an important factor for event decline (Figure 5k, l; Table 1). Given the similarity in the main drivers of $[H^+]$ extremes and marine heatwaves in the subtropical ocean, one can expect that these two univariate extreme events often co-occur. This is indeed the case. Burger et al. (2022) found observation-based evidence for this co-occurrence, indicating that the subtropical oceans are a hotspot for compound high $[H^+]$ and high temperature extremes.

The processes responsible for preconditioning $[H^+]$ extremes, i.e., for increasing $[H^+]$ anomaly before crossing the 90th percentile threshold, have not been analyzed yet. However, the simulated drivers during this preconditioning phase are often similar to those during event onset, with temperature increases from air-sea heat flux dominating in the subtropical oceans and advective increases in carbon dominating in the tropical oceans (supporting information Table S2 and supporting information Figure S10). Therefore, this study's results on the driving mechanisms of $[H^+]$ extreme event onset often also apply to the preceding preconditioning phase.

Even though we consider our results as robust, a number of caveats need to be discussed. The analysis of OAX event drivers relies on data from an Earth system model, as certain processes cannot be independently validated with observational-based data due to its limited availability. The robustness of our results depends therefore on the Earth system model's accuracy in simulating the physical and biogeochemical processes that lead to $[H^+]$ and Ω_A variations and extremes. As these processes also drive spatial variability patterns in $[H^+]$ and Ω_A, a first step is to evaluate simulated variability patterns in the seasonal anomalies of $[H^+]$, Ω_A, and the underlying physical fields T and S against observation-based data (Section 2.2). Overall, we found a good agreement both in the magnitude of variability and in spatial differences for all variables. However, simulated variability in $[H^+]$ anomalies in high latitude regions is lower than in the observation-based data, associated with a low bias in simulated variability of C_T anomalies. The identified lack in simulated C_T variability in these regions suggests a too small contribution from C_T variations and a too large contribution from temperature variations to $[H^+]$ dynamics and thus onset and decline of $[H^+]$ extremes (also found for CMIP6-type models in Burger et al. 2022), regionally reinforced by a positive bias in simulated temperature variability in the Southern Ocean. The identified drivers of Ω_A extremes are less affected by these biases, since Ω_A is less dependent on the balance between temperature and C_T variability. Furthermore, simulated salinity and thus freshwater variations are too large in the western tropical Pacific and Indian Ocean. As a result, evaporation and precipitation may be less important drivers of $[H^+]$ and Ω_A extremes in these regions than identified here. To better constrain the simulated physical and biogeochemical processes, it would be beneficial to compare the identified drivers for the GFDL ESM2M model to those from other Earth system models that can provide the required diagnostic output.

Another shortcoming is that the ocean model used in this study has a relatively coarse spatial resolution and cannot explicitly simulate small-scale circulation features, such as meso- and submesoscale dynamics (S. M. Griffies et al., 2015). Our analysis may therefore underestimate the impact of these small-scale circulation features on the onset and decline of OAX events. Additionally, the coarse resolution of the ocean model limits our analysis to the open ocean, and higher resolution ocean model including improved biogeochemistry would be needed to more accurately represent the drivers in coastal areas (Turi et al., 2018; Terhaar et al., 2019). It should be also noted that the present study focused on the analysis of the mean driving processes over the onset and decline periods of OAX events. However, individual extreme events may be governed by different processes. For example, the drivers in a region can vary between seasons (discussed in Section 3.4), and different types of extremes, characterized by different combinations of drivers, can also occur during the same season (Vogt et al., 2022). The mean process contributions to OAX event onset and decline shown in this study therefore characterize average extremes event in a region and season. Finally, this study analyzes the drivers of OAX events under preindustrial stationary climate conditions. However, ongoing ocean warming and acidification may modify the primary drivers of OAX events, as the background ocean carbon and temperature fields on which the drivers act, as well as the drivers themselves, may change with climate change. To address this limitation, future research should extend our analysis to simulations that include the climate change signal.

In conclusion, our modeling results highlight the crucial role of temperature in driving $[H^+]$ extremes, particularly during summer and in the subtropical oceans. This is primarily attributed to anomalous air-sea heat fluxes and vertical mixing of heat. Furthermore, our results indicate that changes in dissolved inorganic carbon are the dominant driver of low Ω_A extremes, as well as for high $[H^+]$ extremes in equatorial regions and high latitudes during winter, thereby designating these regions as hotspots of compound high $[H^+]$ and low Ω_A extremes. Our findings enhance our current understanding of OAX events in the global ocean and provide a first foundation for regional predictions of such events.

Open Research Section

The GFDL ESM2M model output and analysis scripts used in this study are available under the Zenodo repository (URL), Friedrich A. Burger (DATE OF PUBLICATION). (the repository is underway and the URL and date of publication will be added at the next stage of the review process)

Acknowledgments

FAB and TLF have received funding from the Swiss National Science Foundation (PP00P2_198897) and the European Union's Horizon 2020 research and innovation programme under grant agreement No 820989 (project COMFORT, Our common future ocean in the Earth system — quantifying coupled cycles of carbon, oxygen, and nutrients for determining and achieving safe operating spaces with respect to tipping points). FAB and TLF also thank the CSCS Swiss National Supercomputing Centre for computing resources. The work reflects only the authors' view; the European Commission and their executive agency are not responsible for any use that may be made of the information the work contains.

References

Anderson, J. L., Balaji., V., Broccoli, A. J., Cooke, W. F., Delworth, T. L., Dixon, K. W., … Wyman, B. L. (2004). The new GFDL global atmosphere and land model AM2–LM2: Evaluation with prescribed SST simulations. *J. Clim.*, *17*(24), 4641-4673. doi: 10.1175/JCLI-3223.1

Bednaršek, N., Beck, M. W., Pelletier, G., Applebaum, S. L., Feely, R. A., Butler, R., … Štrus, J. (2022, Jun 21). Natural analogues in ph variability and predictability across the coastal pacific estuaries: Extrapolation of the increased oyster dissolution under increased ph amplitude and low predictability related to ocean acidification. *Environmental Science & Technology*, *56*(12), 9015-9028. Retrieved from https://doi.org/10.1021/acs.est.2c00010 doi: 10.1021/acs.est.2c00010

Bednaršek, N., Feely, R. A., Reum, J. C. P., Peterson, B., Menkel, J., Alin, S. R., & Hales, B. (2014). *Limacina helicina* shell dissolution as an indicator of declining habitat suitability owing to ocean acidification in the california current ecosystem. *Proc. R. Soc. B*, *281*(1785), 20140123. doi: 10.1098/rspb.2014.0123

Bednaršek, N., Tarling, G. A., Bakker, D. C. E., Fielding, S., Jones, E. M., Venables, H. J., ... Murphy, E. J. (2012). Extensive dissolution of live pteropods in the southern ocean. *Nat. Geosci.*, *5*, 881-885. doi: 10.1038/ngeo1635

Bindoff, N., Cheung, W., Kairo, J., Aristegui, J., Guinder, V., Hallberg, R., ... Williamson, P. (2019). Chapter 5: Changing ocean, marine ecosystems, and dependent communities. *IPCC Special Report on the Ocean and Cryosphere (SROCC).*

Bopp, L., Resplandy, L., Orr, J. C., Doney, S. C., Dunne, J. P., Gehlen, M., ... Vichi, M. (2013). Multiple stressors of ocean ecosystems in the 21st century: projections with CMIP5 models. *Biogeosciences*, *10*(10). doi: 10.5194/bg-10-6225-2013

Burger, F. A., John, J. G., & Frölicher, T. L. (2020). Increase in ocean acidity variability and extremes under increasing atmospheric CO_2. *Biogeosciences*, *17*(18), 4633–4662. doi: 10.5194/bg-17-4633-2020

Burger, F. A., Terhaar, J., & Frölicher, T. L. (2022, Aug 16). Compound marine heatwaves and ocean acidity extremes. *Nature Communications*, *13*(1), 4722. Retrieved from https://doi.org/10.1038/s41467-022-32120-7 doi: 10.1038/s41467-022-32120-7

Caldeira, K., & Wickett, M. E. (2003). Anthropogenic carbon and ocean pH. *Nature*, *425*(6956), 365-365. doi: 10.1038/425365a

Canadell, J. G., Monteiro, P. M. S., Costa, M. H., Cotrim da Cunha, L., Cox, P. M., Eliseev, A. V., ... Zickfeld, K. (2021). Global carbon and other biogeochemical cycles and feedbacks. *Climate Change 2021: The Physical Science Basis. Contribution of Working Group I to the Sixth Assessment Report of the Intergovernmental Panel on Climate Change [Masson-Delmotte, V., P. Zhai, A. Pirani, S. L. Connors, C. Péan, S. Berger, N. Caud, Y. Chen, L. Goldfarb, M. I. Gomis, M. Huang, K. Leitzell, E. Lonnoy, J.B.R. Matthews, T. K. Maycock, T. Waterfield, O. Yelekçi, R. Yu and B. Zhou (eds.)]. Cambridge University Press. In Press.*

Carter, B. R., Feely, R. A., Williams, N. L., Dickson, A. G., Fong, M. B., & Takeshita, Y. (2018). Updated methods for global locally interpolated estimation of alkalinity, pH, and nitrate. *Limnol. Oceanogr. Methods*, *16*(2), 119-131. doi: 10.1002/lom3.10232

Deser, C., Alexander, M. A., Xie, S.-P., & Phillips, A. S. (2010). Sea surface temperature variability: Patterns and mechanisms. *Annu. Rev. Mar. Sci.*, *2*(1), 115-143. doi: 10.1146/annurev-marine-120408-151453

Desmet, F., Gruber, N., Köhn, E. E., Münnich, M., & Vogt, M. (2022). Tracking the space-time evolution of ocean acidification extremes in the california current system and northeast pacific. *Journal of Geophysical Research: Oceans*, *127*(5), e2021JC018159. Retrieved from https://agupubs.onlinelibrary.wiley.com/doi/abs/10.1029/2021JC018159 (e2021JC018159 2021JC018159) doi: https://doi.org/10.1029/2021JC018159

Doney, S. C., Busch, D. S., Cooley, S. R., & Kroeker, K. J. (2020). The impacts of ocean acidification on marine ecosystems and reliant human communities. *Annu. Rev. Environ. Resour.*, *45*(1), 83-112. doi: 10.1146/annurev-environ-012320-083019

Doney, S. C., Fabry, V. J., Feely, R. A., & Kleypas, J. A. (2009). Ocean acidification: The other CO_2 problem. *Annual Review of Marine Science*, *1*(1), 169-192. doi: 10.1146/annurev.marine.010908.163834

Doney, S. C., Lima, I., Feely, R. A., Glover, D. M., Lindsay, K., Mahowald, N., ... Wanninkhof, R. (2009). Mechanisms governing interannual variability in upper-ocean inorganic carbon system and air–sea CO_2 fluxes: Physical climate and atmospheric dust. *Deep Sea Res. Part II: Top. Stud. Oceanogr.*, *56*(8), 640-655. doi: https://doi.org/10.1016/j.dsr2.2008.12.006

Dunne, J. P., John, J. G., Adcroft, A. J., Griffies, S. M., Hallberg, R. W., Shevliakova, E., ... Zadeh, N. (2012). GFDL's ESM2 global coupled climate–carbon earth system models. Part I: Physical formulation and baseline simulation characteristics. *J. Clim.*, *25*(19), 6646-6665. doi: 10.1175/JCLI-D-11-00560.1

Dunne, J. P., John, J. G., Shevliakova, E., Stouffer, R. J., Krasting, J. P., Malyshev, S. L., ... Zadeh, N. (2013). GFDL's ESM2 global coupled climate–carbon earth system models. Part II: Carbon system formulation and baseline simulation characteristics. *J. Clim.*, *26*(7), 2247-2267. doi: 10.1175/JCLI-D-12-00150.1

Fassbender, A. J., Rodgers, K. B., Palevsky, H. I., & Sabine, C. L. (2018). Seasonal asymmetry in the evolution of surface ocean pCO_2 and pH thermodynamic drivers and the influence on sea-air CO_2 flux. *Global Biogeochem. Cycles*, *32*(10), 1476-1497. doi: 10.1029/2017GB005855

Fay, A. R., Gregor, L., Landschützer, P., McKinley, G. A., Gruber, N., Gehlen, M., ... Zeng, J. (2021). Seaflux: harmonization of air–sea co_2 fluxes from surface $p\mathrm{co}_2$ data products using a standardized approach. *Earth System Science Data*, *13*(10), 4693–4710. doi: 10.5194/essd-13-4693-2021

Friedlingstein, P., Jones, M. W., O'Sullivan, M., Andrew, R. M., Bakker, D. C. E., Hauck, J., ... Zeng, J. (2022). Global carbon budget 2021. *Earth System Science Data*, *14*(4), 1917–2005. Retrieved from `https://essd.copernicus.org/articles/14/1917/2022/` doi: 10.5194/essd-14-1917-2022

Gnanadesikan, A., Dunne, J. P., & John, J. (2012). Understanding why the volume of suboxic waters does not increase over centuries of global warming in an earth system model. *Biogeosciences*, *9*(3), 1159–1172. doi: 10.5194/bg-9-1159-2012

Good, S. A., Martin, M. J., & Rayner, N. A. (2013). EN4: Quality controlled ocean temperature and salinity profiles and monthly objective analyses with uncertainty estimates. *J. Geophys. Res. Oceans*, *118*(12), 6704-6716. doi: 10.1002/2013JC009067

Griffies, S. (2009). *Elements of MOM4p1* (GFDL OCEAN GROUP TECHNICAL REPORT NO.6). Princeton University Forrestal Campus, 201 Forrestal Road, Princeton, NJ 08540-6649: NOAA/Geophysical Fluid Dynamics Laboratory.

Griffies, S. M., Winton, M., Anderson, W. G., Benson, R., Delworth, T. L., Dufour, C. O., ... Zhang, R. (2015). Impacts on ocean heat from transient mesoscale eddies in a hierarchy of climate models. *Journal of Climate*, *28*(3), 952 - 977. doi: https://doi.org/10.1175/JCLI-D-14-00353.1

Gruber, N., Boyd, P. W., Frölicher, T. L., & Vogt, M. (2021). Ocean biogeochemical extremes and compound events. *Nature, in review*.

Hagens, M., & Middelburg, J. J. (2016). Attributing seasonal pH variability in surface ocean waters to governing factors. *Geophys. Res. Lett.*, *43*(24), 12,528-12,537. doi: https://doi.org/10.1002/2016GL071719

Hauri, C., Gruber, N., McDonnell, A. M. P., & Vogt, M. (2013). The intensity, duration, and severity of low aragonite saturation state events on the california continental shelf. *Geophys. Res. Lett.*, *40*(13), 3424-3428. doi: 10.1002/grl.50618

Hayashida, H., Matear, R. J., & Strutton, P. G. (2020). Background nutrient concentration determines phytoplankton bloom response to marine heatwaves. *Global Change Biology*, *26*(9), 4800–4811. Retrieved from https://onlinelibrary.wiley.com/doi/abs/10.1111/gcb.15255 doi: https://doi.org/10.1111/gcb.15255

Hobday, A. J., Alexander, L. V., Perkins, S. E., Smale, D. A., Straub, S. C., Oliver, E. C., ... Wernberg, T. (2016). A hierarchical approach to defining marine heatwaves. *Prog. Oceanogr.*, *141*, 227-238. doi: https://doi.org/10.1016/j.pocean.2015.12.014

Hofmann, G. E., Smith, J. E., Johnson, K. S., Send, U., Levin, L. A., Micheli, F., ... Martz, T. R. (2011, 12). High-frequency dynamics of ocean pH: A multi-ecosystem comparison. *PloS One*, *6*(12), 1-11. doi: 10.1371/journal.pone.0028983

Jiang, L.-Q., Dunne, J., Carter, B. R., Tjiputra, J. F., Terhaar, J., Sharp, J. D., ... Ziehn, T. (2023). Global surface ocean acidification indicators from 1750 to 2100. *Journal of Advances in Modeling Earth Systems*, *15*(3), e2022MS003563. Retrieved from https://agupubs.onlinelibrary.wiley.com/doi/abs/10.1029/2022MS003563 (e2022MS003563 2022MS003563) doi: https://doi.org/10.1029/2022MS003563

Kroeker, K. J., Kordas, R. L., Crim, R., Hendriks, I. E., Ramajo, L., Singh, G. S., ... Gattuso, J.-P. (2013). Impacts of ocean acidification on marine organisms: quantifying sensitivities and interaction with warming. *Glob. Change Biol.*, *19*(6), 1884-1896. doi: 10.1111/gcb.12179

Kwiatkowski, L., & Orr, J. C. (2018). Diverging seasonal extremes for ocean acidification during the twenty-first century. *Nat. Clim. Change*, *8*(2), 141-145. doi: 10.1038/s41558-017-0054-0

Kwiatkowski, L., Torres, O., Aumont, O., & Orr, J. C. (2023). Modified future diurnal variability of the global surface ocean CO_2 system. *Global Change Biology*, *29*(4), 982-997. Retrieved from https://onlinelibrary.wiley.com/doi/abs/10.1111/gcb.16514 doi: https://doi.org/10.1111/gcb.16514

Kwiatkowski, L., Torres, O., Bopp, L., Aumont, O., Chamberlain, M., Christian, J. R., ... Ziehn, T. (2020). Twenty-first century ocean warming, acidification, deoxygenation, and upper-ocean nutrient and primary production decline from CMIP6 model projections. *Biogeosciences*, *17*(13), 3439–3470. Retrieved from https://bg.copernicus.org/articles/17/3439/2020/ doi: 10.5194/bg-17-3439-2020

Landschützer, P., Gruber, N., & Bakker, D. C. E. (2016). Decadal variations and trends of the global ocean carbon sink. *Global Biogeochem. Cycles*, *30*(10), 1396-1417. doi: 10.1002/2015GB005359

Landschützer, P., Gruber, N., & Bakker, D. C. E. (2022). *An observation-based global monthly gridded sea surface pCO_2 product from 1982 onward and its monthly climatology (NCEI Accession 0160558)* [Dataset]. Retrieved from https://doi.org/10.7289/V5Z899N6

Leinweber, A., & Gruber, N. (2013). Variability and trends of ocean acidification in the southern california current system: A time series from santa monica bay. *J. Geophys. Res. Oceans*, *118*(7), 3622-3633. doi: 10.1002/jgrc.20259

Mogen, S. C., Lovenduski, N. S., Dallmann, A. R., Gregor, L., Sutton, A. J., Bograd, S. J., ... Yeager, S. (2022). Ocean biogeochemical signatures of the north pacific blob. *Geophysical Research Letters*, *49*(9), e2021GL096938. Retrieved from https://agupubs.onlinelibrary.wiley.com/doi/abs/10.1029/2021GL096938 (e2021GL096938 2021GL096938) doi: https://doi.org/10.1029/2021GL096938

Najjar, R., & Orr, J. (1998). *Design of OCMIP-2 simulations of chlorofluorocarbons, the solubility pump and common biogeochemistry* (internal OCMIP report). LSCE/CEA Saclay, Gif-sur-Yvette, France. Retrieved from ocmip5.ipsl.jussieu.fr/OCMIP/phase2/simulations/design.ps

Orr, J. C., & Epitalon, J.-M. (2015). Improved routines to model the ocean carbon-

ate system: mocsy 2.0. *Geosci. Model Dev.*, *8*(3), 485–499. doi: 10.5194/gmd-8-485-2015
Orr, J. C., Epitalon, J.-M., Dickson, A. G., & Gattuso, J.-P. (2018). Routine uncertainty propagation for the marine carbon dioxide system. *Mar. Chem.*, *207*, 84 - 107. doi: doi.org/10.1016/j.marchem.2018.10.006
Orr, J. C., Fabry, V. J., Aumont, O., Bopp, L., Doney, S. C., Feely, R. A., ... Yool, A. (2005). Anthropogenic ocean acidification over the twenty-first century and its impact on calcifying organisms. *Nature*, *437*(7059), 681-686. doi: 10.1038/nature04095
Orr, J. C., Kwiatkowski, L., & Pörtner, H.-O. (2022, Oct 01). Arctic ocean annual high in pCO_2 could shift from winter to summer. *Nature*, *610*(7930), 94-100. Retrieved from `https://doi.org/10.1038/s41586-022-05205-y` doi: 10.1038/s41586-022-05205-y
Palter, J. B., Griffies, S. M., Samuels, B. L., Galbraith, E. D., Gnanadesikan, A., & Klocker, A. (2014). The deep ocean buoyancy budget and its temporal variability. *J. Clim.*, *27*(2), 551 - 573. doi: 10.1175/JCLI-D-13-00016.1
Shevliakova, E., Pacala, S. W., Malyshev, S., Hurtt, G. C., Milly, P. C. D., Caspersen, J. P., ... Crevoisier, C. (2009). Carbon cycling under 300 years of land use change: Importance of the secondary vegetation sink. *Global Biogeochem. Cycles*, *23*(2), 1-16. doi: 10.1029/2007GB003176
Spisla, C., Taucher, J., Bach, L. T., Haunost, M., Boxhammer, T., King, A. L., ... Riebesell, U. (2021). Extreme levels of ocean acidification restructure the plankton community and biogeochemistry of a temperate coastal ecosystem: A mesocosm study. *Frontiers in Marine Science*, *7*, 1240. Retrieved from `https://www.frontiersin.org/article/10.3389/fmars.2020.611157` doi: 10.3389/fmars.2020.611157
Steinacher, M., Joos, F., Frölicher, T. L., Plattner, G.-K., & Doney, S. C. (2009). Imminent ocean acidification in the arctic projected with the ncar global coupled carbon cycle-climate model. *Biogeosciences*, *6*(4), 515–533. Retrieved from `https://bg.copernicus.org/articles/6/515/2009/` doi: 10.5194/bg-6-515-2009
Terhaar, J., Orr, J. C., Ethé, C., Regnier, P., & Bopp, L. (2019). Simulated arctic ocean response to doubling of riverine carbon and nutrient delivery. *Global Biogeochem. Cycles*, *33*(8), 1048-1070. doi: 10.1029/2019GB006200
Torres, O., Kwiatkowski, L., Sutton, A. J., Dorey, N., & Orr, J. C. (2021). Characterizing mean and extreme diurnal variability of ocean CO_2 system variables across marine environments. *Geophys. Res. Lett.*, *48*(5), e2020GL090228. doi: https://doi.org/10.1029/2020GL090228
Turi, G., Alexander, M., Lovenduski, N. S., Capotondi, A., Scott, J., Stock, C., ... Jacox, M. (2018). Response of o_2 and pH to ENSO in the california current system in a high-resolution global climate model. *Ocean Sci.*, *14*(1), 69–86. doi: 10.5194/os-14-69-2018
Vogt, L., Burger, F. A., Griffies, S. M., & Frölicher, T. L. (2022). Local drivers of marine heatwaves: A global analysis with an earth system model. *Frontiers in Climate*, *4*. Retrieved from `https://www.frontiersin.org/articles/10.3389/fclim.2022.847995` doi: 10.3389/fclim.2022.847995
Winton, M. (2000). A reformulated three-layer sea ice model. *J. Atmos. Ocean. Technol.*, *17*(4), 525-531. doi: 10.1175/1520-0426(2000)017⟨0525:ARTLSI⟩2.0.CO;2
Xue, L., Cai, W.-J., Jiang, L.-Q., & Wei, Q. (2021). Why are surface ocean pH and $CaCO_3$ saturation state often out of phase in spatial patterns and seasonal cycles? *Global Biogeochem. Cycles*, *35*(7), e2021GB006949. doi: https://doi.org/10.1029/2021GB006949
Zeebe, R. E., & Wolf-Gladrow, D. (2001). *CO_2 in seawater: Equilibrium, kinetics, isotopes* (R. E. Zeebe & D. Wolf-Gladrow, Eds.). Elsevier, Amsterdam.